

Diapycnal Mixing Induced by Rough Small-Scale Bathymetry

Julia Christin Muchowski¹, Lars Arneborg², Lars Umlauf³, Peter Ludwig Holtermann³, Ezra Eisbrenner⁴, Christoph Humborg⁵, Martin Jakobsson⁶, and Christian Stranne¹

¹Stockholm University

²Swedish Meteorological and Hydrological Institute

³Leibniz-Institute for Baltic Sea Research (IOW)

⁴Department of Meteorology, Stockholm University

⁵Department of Environmental Science and Analytical Chemistry, Stockholm University

⁶Department of Geological Sciences, Stockholm University

December 22, 2022

Abstract

We investigate the effect of extremely rough bathymetry on energy dissipation and mixing in a coastal region characterized by small-scale seafloor features penetrating a strongly-stratified density interface of comparable vertical scale. Our data from the non-tidal Baltic Sea include shear microstructure measurements and observations from a broadband echosounder, here used to resolve the extreme variability and intermittency of stratified turbulence in the vicinity of obstacles. Scale analysis and acoustic imaging of small-scale turbulent motions suggest that the underlying mixing mechanisms are related to topographic wake eddies and, to a smaller extent, to breaking internal waves near the bathymetric features. Vertical diffusivities exceed those at a nearby reference station with smooth bathymetry by up to two orders of magnitude. Our study emphasizes the importance of rough small-scale (< 1 km) bathymetric features for energy dissipation and vertical turbulent transport in coastal areas shaped by e.g., glacial, tectonic, or volcanic processes.

Hosted file

952026_0_art_file_10535355_rn6y9g.docx available at <https://authorea.com/users/568915/articles/614554-diapycnal-mixing-induced-by-rough-small-scale-bathymetry>

Hosted file

952026_0_supp_10535365_rmvpz.docx available at <https://authorea.com/users/568915/articles/614554-diapycnal-mixing-induced-by-rough-small-scale-bathymetry>

1
2
3 **Diapycnal Mixing Induced by Rough Small-Scale Bathymetry**
4

5 **J. Muchowski^{1,2}, L. Arneborg³, L. Umlauf⁴, P. Holtermann⁴, E. Eisbrenner⁵, C.**
6 **Humborg^{1,2}, M. Jakobsson¹ and C. Stranne^{1,2}**

7 ¹ Department of Geological Sciences, Stockholm University, Stockholm, Sweden.

8 ² Baltic Sea Center, Stockholm, Sweden.

9 ³ Department of Research and Development, Swedish Meteorological and Hydrological Institute,
10 Gothenburg, Sweden.

11 ⁴ Leibniz-Institute for Baltic Sea Research, Warnemünde, Germany.

12 ⁵ Department of Meteorology, Stockholm University, Stockholm, Sweden.

13
14 Corresponding author: Julia Muchowski (julia.muchowski@geo.su.se)

15
16 **Key Points:**

- 17 • High-resolution turbulence observations in a shallow, strongly stratified region with
18 extremely rough seafloor topography
- 19 • Acoustic turbulence imaging shows highly intermittent and localized mixing due to wake
20 eddies and internal-wave breaking near obstacles
- 21 • Strongly enhanced mixing due to bathymetric features, causing hotspots of mixing in the
22 Baltic Sea
23

24 Abstract

25 We investigate the effect of extremely rough bathymetry on energy dissipation and mixing in a
26 coastal region characterized by small-scale seafloor features penetrating a strongly-stratified
27 density interface of comparable vertical scale. Our data from the non-tidal Baltic Sea include
28 shear microstructure measurements and observations from a broadband echosounder, here used
29 to resolve the extreme variability and intermittency of stratified turbulence in the vicinity of
30 obstacles. Scale analysis and acoustic imaging of small-scale turbulent motions suggest that the
31 underlying mixing mechanisms are related to topographic wake eddies and, to a smaller extent,
32 to breaking internal waves near the bathymetric features. Vertical diffusivities exceed those at a
33 nearby reference station with smooth bathymetry by up to two orders of magnitude. Our study
34 emphasizes the importance of rough small-scale (< 1 km) bathymetric features for energy
35 dissipation and vertical turbulent transport in coastal areas shaped by e.g., glacial, tectonic, or
36 volcanic processes.

37

38 Plain Language Summary

39 Mixing of water across density interfaces is important for ecosystems and the circulation
40 between basins. However, mixing related to rough small-scale bathymetry is often not resolved
41 in models and difficult to measure. In this study, we show high-resolution acoustic observations
42 of intense vertical mixing across a strong density interface, that separates the saltier bottom water
43 from the fresher surface water in the northern Baltic Sea. In the study region, steep underwater
44 hills and ridges extend into the density interface. As water flows over the region, the hills and
45 ridges cause the water to mix. Measured values of mixing and vertical salt fluxes in this region
46 are up to two orders of magnitude higher than at a nearby reference station with smooth
47 bathymetry. Our analysis suggests that the observed high mixing is mainly caused by eddies in
48 the wake of obstacles and secondarily by breaking internal waves, which are waves within the
49 water that occur on interfaces between layers with different properties. Understanding mixing
50 mechanisms and estimating their contribution is needed to implement mixing into ocean models.
51 This study highlights the importance of rough small-scale seafloor features (< 1 km) for mixing
52 and vertical transport of heat and matter.

53 **Keywords:** diapycnal mixing, rough small-scale bathymetry, stratified flow over obstacles,
54 broadband acoustic observations of turbulent mixing, microstructure profiler turbulence
55 measurements, mixing across halocline

56

57 **1 Introduction**

58 Rough bathymetry is known to considerably increase vertical mixing in the deep ocean (Polzin et
59 al. 1997; Ledwell et al. 2000; Garabato et al. 2004; Kunze et al. 2006; Nikurashin and Legg
60 2011; Waterhouse et al. 2014), in fjords (Arneborg & Jansson, 2017), and in lakes (Wüest &
61 Lorke, 2003). Several mechanisms have been shown to result in enhanced mixing near rough
62 bathymetry. Processes related to internal-wave generation (Alford et al., 2011; Garrett & Kunze,
63 2007; MacKinnon et al., 2017; Nycander, 2005), hydraulic effects (Alford et al., 2013; Arneborg
64 & Jansson, 2017; Legg & Klymak, 2008), and the shedding of eddies in the wake of topographic
65 obstacles (Caldeira et al., 2005; MacKinnon et al., 2019; Pawlak et al., 2003; Perfect et al., 2020)
66 are believed to be particularly relevant. However, field studies of these processes, typically based
67 on in-situ profiling measurements, were generally unable to capture the extreme spatial
68 heterogeneity and intermittency of turbulence near bathymetric features, and focused only on
69 individual obstacles rather than the overall effect in regions with extremely rough bathymetry.

70 Here, we combine traditional turbulence microstructure profiling measurements with a new type
71 of high-resolution broadband acoustic turbulence observations to investigate the effect of
72 extremely rough bathymetry on energy dissipation and mixing in a coastal region characterized
73 by a large number of topographic features (hills and ridges) penetrating into a strongly stratified
74 density interface. Our study area in the Southern Quark, northern Baltic Sea, is known for its
75 rough small-scale bathymetry (Jakobsson et al., 2019) with horizontal scales O_h (100 m) and a
76 large potential for enhanced mixing (Nohr & Gustafsson, 2009). While most previous studies
77 that investigate mixing related to rough bathymetry have focused on tidal currents, we present a
78 dataset practically not influenced by tides. Our study points at the relevance of seafloor-ocean
79 interactions in coastal regions with strongly corrugated bathymetry which lead to enhanced
80 energy dissipation and vertical transports of nutrients and oxygen and therefore may have an
81 important regulatory effect on the development of oxygen minimum zones.

82

83 **2 Study Area and Methods**

84 The study area in the Southern Quark is located at the border between the Bothnian and Åland
85 seas (Fig. 1). It constitutes a major oceanographic bottleneck in which the bathymetry controls
86 water exchange between two of the Baltic Sea's main basins (Elken & Matthäus, 2008). The
87 particularly rough seafloor is due to the underlying bedrock geology, tectonic lineaments
88 (Beckholmen & Tiren, 2009), and interaction between the seafloor and the Scandinavian Ice
89 Sheet (Greenwood et al., 2017). Here we use the gridded bathymetric model compiled by
90 EMODnet at a grid-cell resolution of 1/16 arc minute (EMODnet Bathymetry Consortium, in
91 prep) to assess the seafloor morphology. The version we use is scheduled to be published before
92 the end of 2022 and includes multibeam bathymetry in the Southern Quark acquired with
93 Stockholm University's Research Vessel R/V *Electra* in 2017 (Jakobsson et al., 2019).

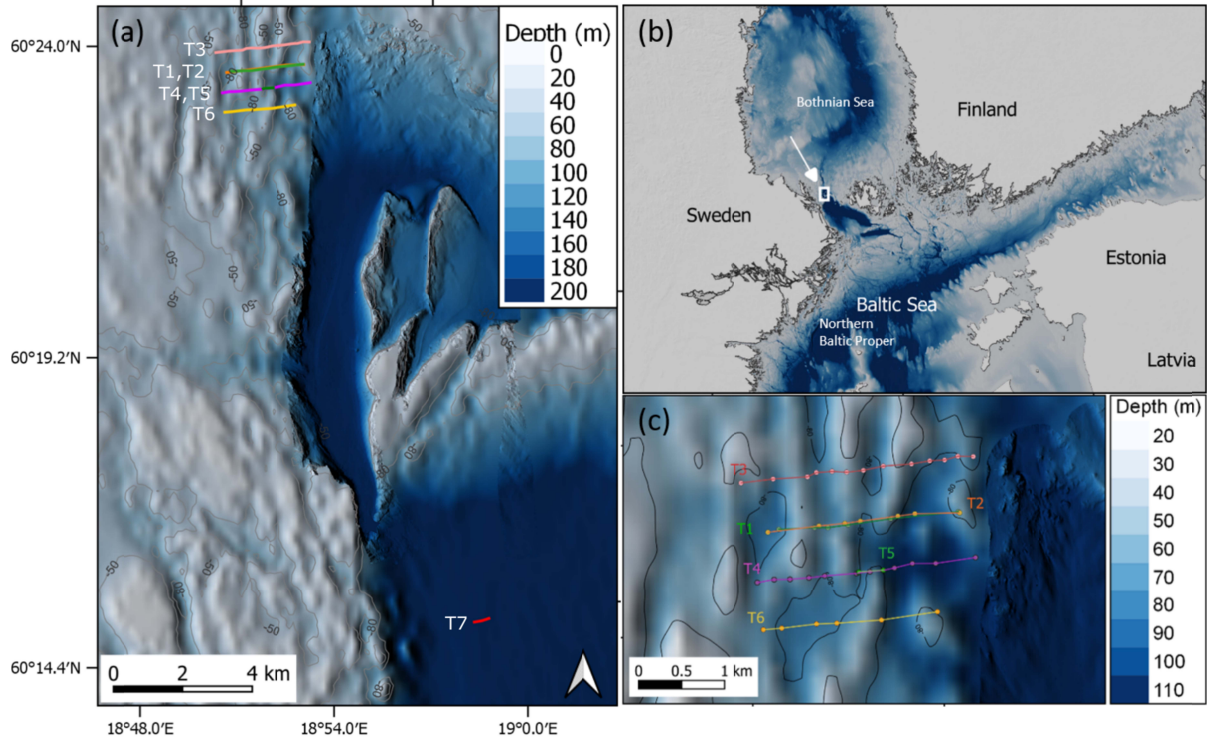
94 Oceanographic and acoustic data presented in this study were collected during a cruise with R/V
95 *Electra* on 2-3 March 2020 on six transects in a region of particularly rough bathymetry and a
96 reference station located in a deeper and topographically smooth basin bounding the study area
97 in the east and south (Fig. 1). Oceanographic data were collected with a free-falling MSS-90L
98 microstructure profiler (MSS) from Sea&Sun Technology (SST, Germany), equipped with two
99 PNS06 airfoil shear probes for estimates of the dissipation rate of turbulent kinetic energy, a
100 FP07 fast-response thermistor, precision CTD (Conductivity, Temperature, Depth) sensors, and
101 an oxygen sensor. All sensors were sampled at 1024 Hz and digitized at 16-bit resolution. The
102 sinking velocity of the profiler was adjusted to about 0.7 m s^{-1} . In total, 50 MSS casts were
103 collected, of which 47 casts are located in the study region and three casts at the reference station
104 (Fig. 1 a and c). From the MSS profiles, conservative temperature θ , absolute salinity S_A , and
105 buoyancy frequency N were computed according to the international TEOS-10 standard for
106 seawater (IOC et al. 2010). Detailed information on the processing of MSS shear microstructure
107 data is found in (Muchowski et al., 2022). The location of the transects and positioning of the
108 MSS casts was based on real-time acoustic observations as described in the next section.

109 Acoustic observations were conducted with a Simrad ES70-7C (45-90 kHz) split beam
110 transducer (Kongsberg, Norway) in combination with a Simrad EK80 wideband transceiver,
111 using a ping rate of 1 Hz and a pulse duration of 4.1 ms. The received signal was processed using
112 pulse compression and compensated for spherical spreading and absorption. The system was
113 calibrated in the study area during the measuring campaign with a 38.1-mm tungsten carbide

114 sphere, as described in Demer et al. (2015). R/V *Electra*'s Seapath 330+ RTK GPS unit and a
115 MRU5+ motion sensor were used for accurate positioning and compensation of (wave-induced)
116 heave in the acoustic observations. We show calibrated acoustic backscatter strength per volume
117 (S_v) in dB re 1 μ Pa.

118 While the MSS profiler measures small-scale turbulent velocity fluctuations, the EK80 measures
119 acoustic backscatter from density and sound speed fluctuations, caused by temperature and
120 salinity fluctuations (e.g. Lavery et al. 2013). Therefore, acoustics only register turbulent
121 structures in regions with existing background temperature and salinity gradients, where
122 turbulent stirring induces temperature and salinity microstructure and thus increased acoustic
123 backscatter (Muchowski et al., 2022), whereas MSS measurements show dissipation rates also in
124 well-mixed parts of the water column. Thus, the acoustic observations indicate regions where
125 mixing of different water masses occurs and where the diapycnal transport of salt and/or heat is
126 increased. Additionally, the EK80 records strong backscatter from biological scatterers, such as
127 zooplankton and fish, in this dataset. Muchowski et al. (2022) showed that in areas where
128 biological scattering does not dominate the signal, turbulent microstructure is the primary source
129 of acoustic backscatter recorded with the R/V *Electra* EK80 system in this region and time of
130 year. In this study, we conducted acoustic surveys to identify regions of increased stratified
131 mixing prior to our MSS measurements. These real-time acoustic observations enabled us to plan
132 positions of the MSS measurements and to target local mixing hotspots in a region with complex
133 and highly intermittent turbulence.

134 Acoustic Doppler Current Profiler (ADCP) data were collected using *Electra*'s hull-mounted 600
135 kHz Workhorse ADCP (Teledyne RDI, USA) (see Supplementary Fig. S1). This instrument
136 provided reliable data down to 40-50 m water depth and therefore did not include most of the
137 halocline region below approximately 50 m depth.



138

139 *Figure 1: Bathymetry of the study area in the Åland Sea: (a) Overview map with MSS transects T1-T7 marked by colored lines*
 140 *(MSS casts 76-125, collected between 2 March 2020, 14:45 UTC and 3 March 2020, 17:10 UTC). (b) overview map of northern*
 141 *Baltic Sea with study region in the Åland Sea shown in (a) marked by white rectangle; (c) main study region with transects T1-T8*
 142 *enlarged. Each dot represents a MSS cast. Background bathymetry data from EMODnet (EMODnet Bathymetry Consortium*
 143 *2020), detailed multibeam bathymetry data in (a) and (c) acquired by R/V Electra and granted public release by the Swedish*
 144 *Maritime Administration (release 17-03187).*

145 To estimate turbulent mixing, the turbulent vertical diffusion coefficient k_z is calculated from the
 146 dissipation rate of turbulent kinetic energy ε , following the Osborn (1980) model:

$$147 \quad k_z = \gamma \varepsilon N^{-2}, \quad (1)$$

148 where N is the buoyancy frequency of the background stratification and γ the flux coefficient,
 149 here assumed to be equal to 0.2 (Gregg et al., 2018).

150 The vertical transport due to turbulent mixing, F_{zX} , of a tracer, X (e.g. salinity, heat, oxygen,
 151 nutrients) is calculated from Fick's law

$$152 \quad F_{zX} = -k_z \cdot \frac{\partial X}{\partial z} \cdot \rho, \quad (2)$$

153 where z is defined positive upward and ρ is the water density.

154 **3 Results and Discussion**

155 **3.1 In-situ measurements**

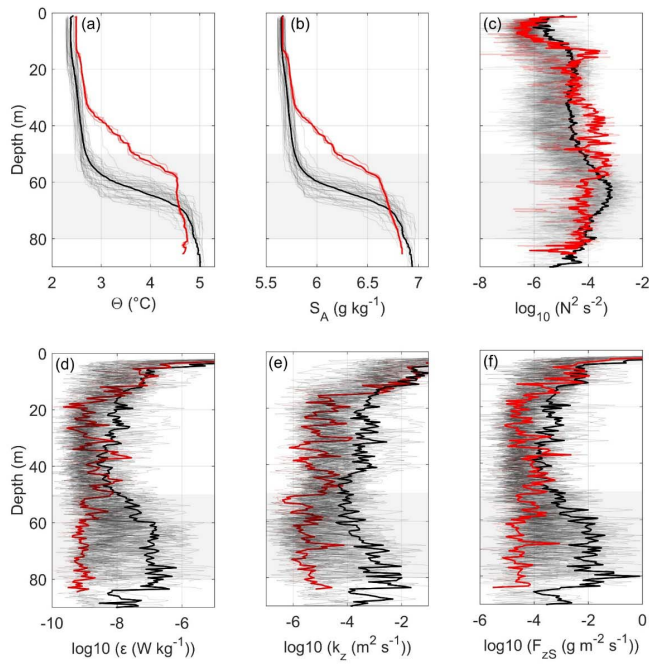
156 Microstructure (MSS) profiles of conservative temperature Θ , absolute salinity S_A , and buoyancy
 157 frequency N show that the stratification in the study area (transect T1-T7, Fig. 1c) is
 158 characterized by a halocline between 50-80 m water depth, which separates warmer and saltier
 159 deep water from a cooler and fresher surface layer (Fig. 2). The entire water column is stably
 160 stratified with a buoyancy frequency that ranges from $N^2 = 10^{-6} \text{ s}^{-2}$ in the surface- and bottom
 161 layers to $N^2 = 10^{-3} \text{ s}^{-2}$ in the halocline.

162 To isolate the effect of the corrugated topography in the study area, we compare our data to
 163 reference transect T7, south of the study region (Fig. 1a, in red), where we expect a similar
 164 meteorological forcing but no significant topographic effects due to the larger water depth and
 165 the smooth seafloor. At this reference station, the halocline is shallower and broader but shows
 166 comparable maximum values for N^2 (Fig. 2). The vertical offset in halocline depth implies a
 167 baroclinic pressure gradient favoring a northward transport of deep water. This transport, and the
 168 mixing processes studied in the following, are important components of the estuarine circulation
 169 of the Northern Baltic Sea, determining water mass properties and ventilation of the deep water.

170 MSS profiles of kinetic energy dissipation rates, ε , vertical turbulent diffusivity, k_z , and vertical
 171 salt flux, F_{zS} , show that all three quantities are increased by up to two orders of magnitude in the
 172 halocline of the study region (Fig. 2d-f). The average dissipation rate in the halocline of all 47
 173 MSS profiles in the study region is $\approx 1.1 \cdot 10^{-7} \text{ W kg}^{-1}$ and thereby two orders of magnitude above
 174 measurements at the reference station. Average vertical diffusivities are $\approx 7 \cdot 10^{-4} \text{ m}^2 \text{ s}^{-1}$ in the
 175 halocline of the study area, while average vertical diffusivities at the reference station as well as
 176 in other parts of the Baltic Sea are measured to be 1-2 orders of magnitude lower. For example,
 177 $k_z < 10^{-5} \text{ m}^2 \text{ s}^{-1}$ in the halocline of the Eastern Gotland Basin (Lass, 2003). The mean salinity flux
 178 through the halocline (50-80 m depth), calculated from (2) and averaged over all MSS profiles in
 179 the study region is $F_{zS} = 0.01 \text{ kg m}^{-2} \text{ s}^{-1}$. While salinities in the study area are overall lower than
 180 in the Baltic Proper, the diapycnal salinity flux is one order of magnitude above the average in

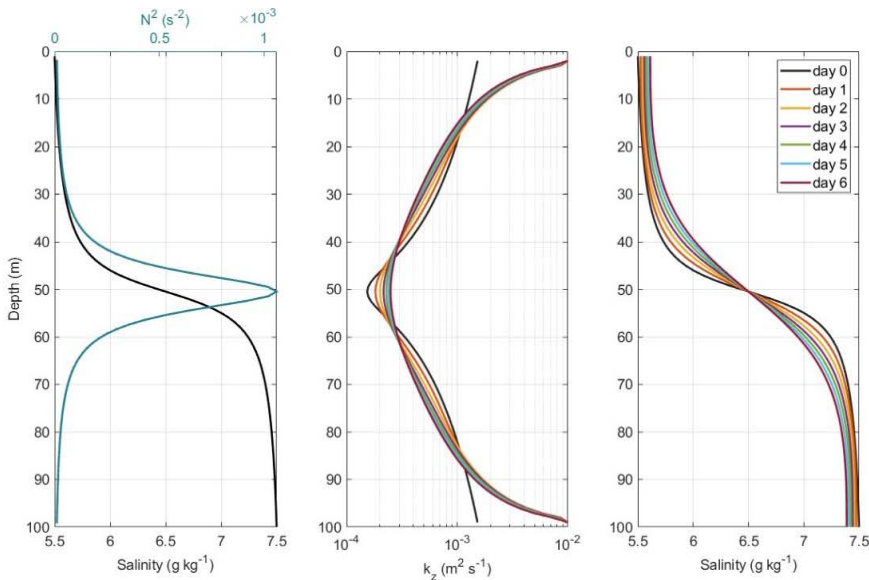
181 the entire Baltic Sea, including upwelling (Reissmann et al. 2009), as well as in the Bornholm
182 (van der Lee & Umlauf, 2011) and Eastern Gotland Basin (Rahm 1985).

183 To investigate the impact of the observed mixing rates on the evolution of the halocline and the
184 adjacent surface and deep-water layers, we numerically solved the one-dimensional diffusion
185 equation with a vertically variable diffusivity, approximated as $k = \min(\alpha N^{-1}, k_{\max})$ (Stigebrandt
186 1987, equation 2.2), with $\alpha = 5 \cdot 10^{-6}$ and $k_{\max} = 10^{-2} \text{ m}^2 \text{ s}^{-1}$. With these parameters, the model
187 reproduces the observed diffusivities in the halocline, and has the advantage, compared to a
188 model with a prescribed (fixed) diffusivity profile, that the diffusivity dynamically adapts to the
189 evolution of the halocline. The initial conditions are chosen to approximate the observed salinity
190 profile by an inverse tangent function. Model results show (Fig. 3) that the halocline width
191 nearly doubles and that salinities in the layers above and below the halocline are modified by
192 about 0.1 g kg^{-1} over a period of 5 days, which would correspond to a typical residence time for
193 surface-layer waters in the study area (horizontal scale: 20 km) for typical current speeds of 0.05
194 m s^{-1} (see supplementary Fig. S1). As the larger-scale forcing of deep-water flow in the area is
195 predominantly northward, the modification of the water below the halocline due to the observed
196 mixing may be relevant for the deep-water conditions in the Bothnian Sea, adjacent to the north
197 of the study region.



198

199 *Figure 2: (a) Conservative temperature (Θ), (b) absolute salinity (S_A), (c) buoyancy frequency (N^2), (d) dissipation rate of*
 200 *turbulent kinetic energy (ϵ), (e) vertical turbulent diffusivity (k_z) and vertical salt flux (F_{zs}) from 47 MSS casts in the study region*
 201 *(black) and 3 MSS casts at the reference station (red) together with their arithmetic mean values (bold). Positions of MSS casts*
 202 *are shown on map in Fig. 1 (MSS 76-125). Grey shaded patch marks the halocline in the study region.*
 203

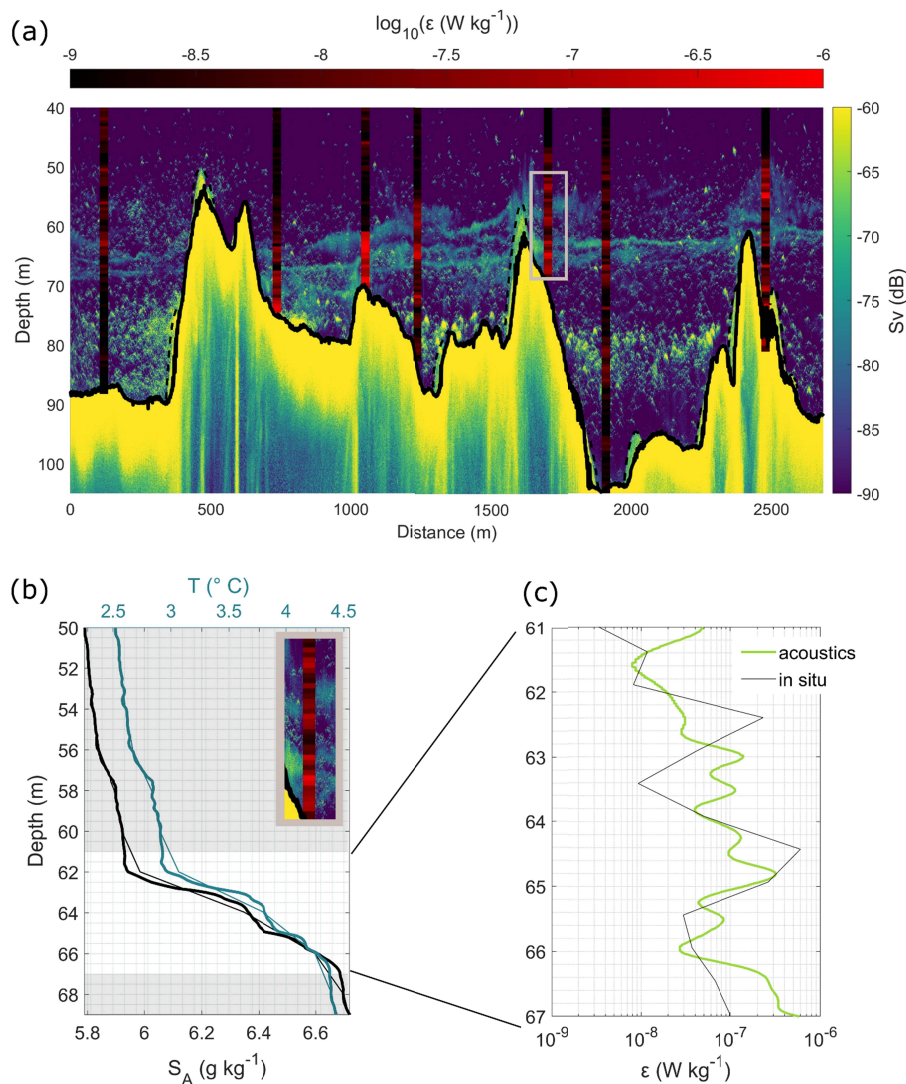


204

205 *Figure 3: Diffusion model of the study region. (a) initial salinity profile and corresponding buoyancy frequency, (b) initial*
 206 *turbulent vertical diffusivity profile (blue) and its development over time, (c) initial salinity profile (blue) and its development*
 207 *over time.*

208 **3.2 Broadband acoustic observations**

209 The unique advantage of acoustic observations compared to the traditional microstructure
 210 profiling described above lies in their extreme spatial resolution, revealing the complex geometry
 211 and intermittency of mixing near topographic obstacles in a level of detail usually available only
 212 from turbulence-resolving numerical simulations (Puthan et al., 2022). Figure 4 shows that
 213 mixing in our study area occurs in confined regions, especially near hilltops that reach into the
 214 halocline and in detached mixing bands that are horizontally correlated on scales of 0.1 – 1 km.
 215 Overall, we see an excellent one-to-one correspondence between regions with enhanced acoustic
 216 backscatter and enhanced energy dissipation from shear microstructure (Fig. 4a), and in some
 217 cases also good quantitative agreements in the inferred dissipation rates (Fig. 4c) in all six
 218 transects (not shown here).



219
 220 *Figure 4: (a) EK80 echogram showing transect T2, sampled 3 March 2020, 09:08-10:00 UTC, with seafloor bathymetry marked in*
 221 *black, sidelobes marked by dashed black line. Vertical profiles show dissipation rates from MSS casts 82-88, color-coded in red.*

222 (b) conservative temperature (turquoise) and absolute salinity (black) profile from MSS 86, (c) dissipation rate ϵ from MSS cast
 223 86 (black) and inferred from acoustic backscatter (green) in combination with temperature and salinity profile shown in (b).
 224

225 Quantitative estimates of energy dissipation rates from acoustic observations in between
 226 microstructure profiles are complicated by the lack of commensurate observations of temperature
 227 and salinity stratification (extrapolations are highly inaccurate due to the strong spatial variability
 228 in this region). Additionally, the acoustic signal is often dominated by biological scattering,
 229 especially in the deeper layers below 70 m. We therefore avoid quantitative estimates and
 230 integration of dissipation rates based on acoustic backscatter. Nevertheless, the acoustic
 231 measurements provide a tool to visualize and map turbulent mixing at high resolution which
 232 would not be achievable with any of the traditional techniques to observe turbulence.

233 **3.3 Mixing mechanisms**

234 Local mixing hotspots seen in Figure 4 are likely caused by a combination of mixing
 235 mechanisms related to the rough bathymetric features. To analyze the relevance of different
 236 potential mixing mechanisms, we define the most important bulk parameters characterizing the
 237 study area: $h = 20$ m as a typical vertical scale of the bathymetric features (as seen in Fig. 4a), L_N
 238 $= 30$ m as the thickness of the halocline (Fig. 2b), $N = 0.015$ s⁻¹ for the average buoyancy
 239 frequency in the halocline (Fig. 2c), $f = 1.26 \cdot 10^{-4}$ s⁻¹ for the Coriolis parameter, and $u =$
 240 0.05 m s⁻¹ for typical velocities at the bottom of the ADCP range, i.e. at the upper end of the
 241 halocline region (see Supplementary Fig. S1). The latter estimate is the most uncertain as the
 242 currents are fluctuating and measurements in the core of the halocline are lacking. Finally, the
 243 lateral scales of bathymetric features in this study are anisotropic, ranging from values of the
 244 order $d = 500$ m in the cross-ridge (west-east) direction to $d = 2000$ m in the along-ridge (north-
 245 south) direction, respectively (Fig. 1c).

246 Based on the above defined parameters, the non-dimensional topographic Froude number
 247 $Fr = u/(Nh)$ can be estimated to ≈ 0.17 . The small Froude number suggests that much of the
 248 flow is blocked or, where possible, flows around the bathymetric features. Near the hilltops,
 249 however, overflow could be possible. The Rossby number is $Ro = u/(fd) \approx 0.2 - 0.8$, where
 250 the smaller and larger values of Ro correspond to our along-ridge and cross-ridge estimates of d .
 251 These small to moderate values suggest that the flow is significantly affected by rotation. The
 252 intrinsic frequency of lee waves, $\omega = 2\pi u/d$, is about $(1.6 - 6.3) \cdot 10^{-4}$ s⁻¹ which is larger than f

253 but much smaller than N , meaning that lee waves are possible but propagate with nearly
 254 horizontal phase lines. Possible mixing mechanisms are therefore to some extent breaking
 255 internal lee waves due to flow over bathymetric features, but more importantly, lee vortices or
 256 wake eddies due to flow around them and nonlinear hydraulic effects due to topographic
 257 blocking. Our observations show similarities to model studies of wake eddies from Puthan et al.
 258 (2020 and 2022), carried out at a topographic Froude number of 0.2 and 0.15, respectively but
 259 for a single hill and at a much larger Rossby number where rotation is less important. Puthan et
 260 al. (2022) pointed out that consistently higher dissipation rates are observed inside the thin
 261 hydraulic jet evolving at the apex of an obstacle for low Fr (see their figure 7). The thin, banded
 262 structures of enhanced backscatter visible in both our EK80 and shear-microstructure
 263 measurements near the top of obstacles (Fig. 4) could be interpreted as evidence for this process
 264 (unfortunately, our ship ADCP data do not reach down to this region).

265

266 These qualitative arguments can be substantiated with the help of shear microstructure
 267 measurements and theoretical energy dissipation estimates. Energy dissipation due to
 268 topographic wake eddies is suggested to scale as u^3/d (e.g., Puthan et al. 2022), yielding
 269 dissipation rates in the range $[0.6 - 2.5] \cdot 10^{-7} \text{ W kg}^{-1}$, i.e. of the same order of magnitude as our
 270 observations ($\approx 1.1 \cdot 10^{-7} \text{ W kg}^{-1}$). The integrated dissipation rate (based on the average
 271 dissipation rate $\bar{\epsilon}$ of all 47 MSS profiles) in the halocline of the study region is

272

$$273 \quad D_i = \int_{z=50 \text{ m}}^{z=80 \text{ m}} \bar{\epsilon} \rho \, dz \approx 3.4 \text{ mW m}^{-2} . \quad (3)$$

274

275 Assuming that the dissipation rate scaling u^3/d is relevant for the halocline, the depth integrated
 276 dissipation, corresponding to (3), would scale as $\rho u^3 L_N/d$, where L_N is the thickness of the
 277 halocline. With the parameters defined above, the resulting integrated dissipation rates are in the
 278 range $[1.3-5.2] \text{ mW m}^{-2}$, close to the observed value. Note that this parametrization for wake
 279 eddies is independent of stratification.

280 Integrated energy dissipation due to internal wave generation at topography in the ocean and the
 281 atmosphere is suggested to scale as $\rho N u^2 h^2/d$ in the linear limit, e.g. (Arneborg & Jansson,
 282 2017; St. Laurent et al., 2002; Stigebrandt, 1976; Welch et al., 2001) and includes stratification.
 283 Using this scaling results in values of D_i in the range $[8-31] \text{ mW m}^{-2}$, i.e. larger than the

284 observed value (3). Previous studies of tidal stratified flow over steep topography (Arneborg &
285 Jansson, 2017; St. Laurent et al., 2002) have shown that about 20% to 30% of the energy flux
286 calculated with this scaling is dissipated locally. This leads to estimates of D_i in the right order of
287 magnitude as (3), with more comparable values for horizontal scales of 2000 m. Studies of
288 atmospheric lee-waves also show a strong decrease in integrated energy conversion to lee waves
289 relative to the linear limit for small Froude numbers (e.g. Welch et al. 2001) which means that
290 the observed value can be in agreement with those results. There are, however, no clear signs of
291 oblique bands that would be expected from breaking internal lee waves. This suggests either that
292 these are not present or that they are horizontal due to the perpendicular transect relative to the
293 northward flow.

294

295 **4 Conclusions**

296 We present in-situ microstructure measurements of dynamic turbulent diapycnal mixing near
297 steep small-scale bathymetric hills and ridges that reach into stratified flow. Collocated acoustic
298 observations of stratified mixing are consistent with shear-microstructure measurements but have
299 much higher vertical and horizontal resolution. Thus, providing insights into the complex
300 anatomy of the mixing, including hotspots of mixing near the summits and crests of the
301 particularly rough bathymetric features. The acoustic observations thereby enable us to map
302 turbulent mixing at unprecedented resolution and to plan in-situ measurements accordingly. We
303 suggest that the observed mixing mechanisms, which here increase dissipation rates by one to
304 two orders of magnitude, could play an important role beyond our study region, such as in large
305 parts of the Bothnian Sea as well as coastal areas in the Baltic Sea and around the globe where
306 rough, small-scale bathymetry reaches into stratified flow.

307

308 Energy conversion and turbulence scalings for both, topographic wake eddies and internal
309 waves, are to some degree supported by our integrated measured dissipation rates. However, the
310 acoustically observed thin, horizontal, laterally coherent bands of high dissipation are similar to
311 what has been shown for idealized stratified flow around seamounts. Additionally, the estimated
312 Froude number of 0.17 points towards the process of wake eddy generation from flow around
313 obstacles more than that of breaking lee waves from flow over obstacles. This could have large
314 impacts on parametrizations, as the scaling of energy dissipation due to wake eddies is

315 fundamentally different from that of internal wave generation, which has usually been assumed
316 to cause mixing above rough seafloor topography. Besides the potential to improve
317 parameterizations of this kind of mixing in models which do not resolve the flow above such
318 bathymetry, a better understanding of the underlying mechanisms may even lead to improved
319 drag parameterizations and thereby more accurate currents and transports in the models, as has
320 been shown to be the case for atmospheric models (Alexander et al., 2010).

321 The combination of a bathymetry roughness index based on high-resolution multibeam data with
322 suitable mixing parameterizations based on stratification and current velocities could potentially
323 improve the ocean component of global, regional, and coastal climate models significantly.

324

325 More observational data as well as model studies of stratified flow over small-scale bathymetry
326 are needed to fully capture the extent of the described processes, discriminate between them and
327 gauge their importance. Future studies could involve a portable autonomous broadband
328 echosounders, either towed, mounted on a CTD rosette, or mounted on gliders for measurements
329 at greater depths.

330

331 **Acknowledgments**

332 We thank Martin Sass (IOW, Warnemunde, Germany) for technical support with MSS profilers
333 during the cruise. We thank Florian Roth, Ole Pinner and Emelie Ståhl for participating in data
334 collection. We thank the captain Thomas Strömsnäs and the crew Mattias Murphy, Carl-Magnus
335 Wiltén and Albin Knochenhauer of R/V Electra for their assistance and support.

336

337 **Open Research**

338 Data will be published and made accessible for downloading on the Bolin Centre Database
339 website (<https://bolin.su.se/data>) prior to publication. Data are already now available on the
340 Bolin Centre Database in the unpublished project:

341 [https://bolin.su.se/data/contributions/?d=8761&p=MjAyMi0xMi0xNiAwOT01Njo1Ny42Mzcx](https://bolin.su.se/data/contributions/?d=8761&p=MjAyMi0xMi0xNiAwOT01Njo1Ny42MzcxMTYgNDQ4MDMyMTE)
342 [MTYgNDQ4MDMyMTE](https://bolin.su.se/data/contributions/?d=8761&p=MjAyMi0xMi0xNiAwOT01Njo1Ny42MzcxMTYgNDQ4MDMyMTE)

343

344 **References**

- 345 Alexander, M. J., Geller, M., McLandress, C., Polavarapu, S., Preusse, P., Sassi, F., Sato, K., Eckermann, S., Ern,
346 M., & Hertzog, A. (2010). Recent developments in gravity-wave effects in climate models and the global
347 distribution of gravity-wave momentum flux from observations and models. *Quarterly Journal of the Royal*
348 *Meteorological Society*, *136*(650), 1103–1124.
- 349 Alford, M. H., Girton, J. B., Voet, G., Carter, G. S., Mickett, J. B., & Klymak, J. M. (2013). Turbulent mixing and
350 hydraulic control of abyssal water in the Samoan Passage. *Geophysical Research Letters*, *40*(17), 4668–
351 4674. <https://doi.org/10.1002/grl.50684>
- 352 Alford, M. H., MacKinnon, J. A., Nash, J. D., Simmons, H., Pickering, A., Klymak, J. M., Pinkel, R., Sun, O.,
353 Rainville, L., Musgrave, R., Beitzel, T., Fu, K.-H., & Lu, C.-W. (2011). Energy Flux and Dissipation in
354 Luzon Strait: Two Tales of Two Ridges. *Journal of Physical Oceanography*, *41*(11), 2211–2222.
355 <https://doi.org/10.1175/JPO-D-11-073.1>
- 356 Arneborg, L., & Jansson, R. (2017). Tidal Energy Loss, Internal Tide Radiation, and Local Dissipation for Two-
357 Layer Tidal Flow over a Sill. *JOURNAL OF PHYSICAL OCEANOGRAPHY*, *47*, 18.
- 358 Beckholmen, M., & Tiren, S. A. (2009). *The geological history of the Baltic Sea. A review of the literature and*
359 *investigation tools*. <https://www.osti.gov/etdeweb/biblio/963502>
- 360 Caldeira, R. M. A., Marchesiello, P., Nezlin, N. P., DiGiacomo, P. M., & McWilliams, J. C. (2005). Island wakes in
361 the Southern California Bight. *Journal of Geophysical Research: Oceans*, *110*(C11).
362 <https://doi.org/10.1029/2004JC002675>
- 363 Demer, D. A., Berger, L., Bernasconi, M., Bethke, E., Boswell, K., Chu, D., Domokos, R., Dunford, A., Fassler, S.,
364 Gauthier, S., Hufnagle, L. T., Jech, J. M., Bouffant, N., Lebourges-Dhaussy, A., Lurton, X., Macaulay, G.
365 J., Perrot, Y., Ryan, T., Parker-Stetter, S., ... Williamson, N. (2015). *Calibration of acoustic instruments*.
366 [Report]. International Council for the Exploration of the Sea (ICES). <https://doi.org/10.25607/OBP-185>
- 367 Elken, J., & Matthäus, W. (2008). Assessment of Climate Change for the Baltic Sea Basin. *Baltic Sea*
368 *Oceanography*, 379–385.
- 369 EMODnet Bathymetry Consortium (2020): EMODnet Digital Bathymetry (DTM).
370 <https://doi.org/10.12770/bb6a87dd-e579-4036-abe1-e649cea9881a>

- 371 Garabato, A. C. N., Polzin, K. L., King, B. A., Heywood, K. J., & Visbeck, M. (2004). Widespread Intense
372 Turbulent Mixing in the Southern Ocean. *Science*, *303*(5655), 210–213.
373 <https://doi.org/10.1126/science.1090929>
- 374 Garrett, C., & Kunze, E. (2007). Internal tide generation in the deep ocean. *Annu. Rev. Fluid Mech.*, *39*, 57–87.
- 375 Greenwood, S. L., Clason, C. C., Nyberg, J., Jakobsson, M., & Holmlund, P. (2017). The Bothnian Sea ice stream:
376 Early Holocene retreat dynamics of the south-central Fennoscandian Ice Sheet. *Boreas*, *46*(2), 346–362.
377 <https://doi.org/10.1111/bor.12217>
- 378 Gregg, M. C., D'Asaro, E. A., Riley, J. J., & Kunze, E. (2018). Mixing Efficiency in the Ocean. *Annual Review of*
379 *Marine Science*, *10*(1), 443–473. <https://doi.org/10.1146/annurev-marine-121916-063643>
- 380 IOC, SCOR and IAPSO, 2010: The international thermodynamic equation of seawater - 2010: Calculation
381 and use of thermodynamic properties. Intergovernmental Oceanographic Commission, Manuals and Guides
382 No. 56, UNESCO (English), 196 pp.
- 383 Jakobsson, M., Stranne, C., O'Regan, M., Greenwood, S. L., Gustafsson, B., Humborg, C., & Weidner,
384 E. (2019). Bathymetric properties of the Baltic Sea. *Ocean Science*, *15*(4), 905–924.
385 <https://doi.org/10.5194/os-15-905-2019>
- 386 Kunze, E., Firing, E., Hummon, J. M., Chereskin, T. K., & Thurnherr, A. M. (2006). Global Abyssal Mixing
387 Inferred from Lowered ADCP Shear and CTD Strain Profiles. *Journal of Physical Oceanography*, *36*(8),
388 1553–1576. <https://doi.org/10.1175/JPO2926.1>
- 389 Lass, H. U. (2003). Dissipation in the Baltic proper during winter stratification. *Journal of Geophysical Research*,
390 *108*(C6), 3187. <https://doi.org/10.1029/2002JC001401>
- 391 Lavery, A. C., Geyer, W. R., & Scully, M. E. (2013). Broadband acoustic quantification of stratified turbulence. *The*
392 *Journal of the Acoustical Society of America*, *134*(1), 40–54. <https://doi.org/10.1121/1.4807780>
- 393 Ledwell, J. R., Montgomery, E. T., Polzin, K. L., St. Laurent, L. C., Schmitt, R. W., & Toole, J. M. (2000).
394 Evidence for enhanced mixing over rough topography in the abyssal ocean. *Nature*, *403*(6766), 179–182.
395 <https://doi.org/10.1038/35003164>
- 396 Legg, S., & Klymak, J. (2008). Internal Hydraulic Jumps and Overturning Generated by Tidal Flow over a Tall
397 Steep Ridge. *Journal of Physical Oceanography*, *38*(9), 1949–1964.
398 <https://doi.org/10.1175/2008JPO3777.1>

- 399 MacKinnon, J. A., Alford, M. H., Voet, G., Zeiden, K. L., Shaun Johnston, T. M., Siegelman, M., Merrifield, S., &
400 Merrifield, M. (2019). Eddy Wake Generation From Broadband Currents Near Palau. *Journal of*
401 *Geophysical Research: Oceans*, *124*(7), 4891–4903. <https://doi.org/10.1029/2019JC014945>
- 402 MacKinnon, J. A., Zhao, Z., Whalen, C. B., Waterhouse, A. F., Trossman, D. S., Sun, O. M., Laurent, L. C. S.,
403 Simmons, H. L., Polzin, K., Pinkel, R., Pickering, A., Norton, N. J., Nash, J. D., Musgrave, R., Merchant,
404 L. M., Melet, A. V., Mater, B., Legg, S., Large, W. G., ... Alford, M. H. (2017). Climate Process Team on
405 Internal Wave–Driven Ocean Mixing. *Bulletin of the American Meteorological Society*, *98*(11), 2429–
406 2454. <https://doi.org/10.1175/BAMS-D-16-0030.1>
- 407 Muchowski, J., Umlauf, L., Arneborg, L., Holtermann, P., Weidner, E., Humborg, C., & Stranne, C. (2022).
408 Potential and Limitations of a Commercial Broadband Echosounder for Remote Observations of Turbulent
409 Mixing. *Journal of Atmospheric and Oceanic Technology*.
- 410 Nikurashin, M., & Legg, S. (2011). A Mechanism for Local Dissipation of Internal Tides Generated at Rough
411 Topography. *Journal of Physical Oceanography*, *41*(2), 378–395. <https://doi.org/10.1175/2010JPO4522.1>
- 412 Nohr, C., & Gustafsson, B. G. (2009). Computation of energy for diapycnal mixing in the Baltic Sea due to internal
413 wave drag acting on wind-driven barotropic currents. *OCEANOLOGIA*, *51*(4), 461–494.
414 <https://doi.org/10.5697/oc.51-4.461>
- 415 Nycander, J. (2005). Generation of internal waves in the deep ocean by tides. *Journal of Geophysical Research:*
416 *Oceans*, *110*(C10). <https://doi.org/10.1029/2004JC002487>
- 417 Pawlak, G., MacCready, P., Edwards, K. A., & McCabe, R. (2003). Observations on the evolution of tidal vorticity
418 at a stratified deep water headland. *Geophysical Research Letters*, *30*(24).
419 <https://doi.org/10.1029/2003GL018092>
- 420 Perfect, B., Kumar, N., & Riley, J. J. (2020). Energetics of Seamount Wakes. Part I: Energy Exchange. *Journal of*
421 *Physical Oceanography*, *50*(5), 1365–1382. <https://doi.org/10.1175/JPO-D-19-0105.1>
- 422 Polzin, K. L., Toole, J. M., Ledwell, J. R., & Schmitt, R. W. (1997). Spatial variability of turbulent mixing in the
423 abyssal ocean. *Science*, *276*, 93–96.
- 424 Puthan, P., Jalali, M., Ortiz-Tarin, J. L., Chongsiripinyo, K., Pawlak, G., & Sarkar, S. (2020). The wake of a three-
425 dimensional underwater obstacle: Effect of bottom boundary conditions. *Ocean Modelling*, *149*, 101611.
426 <https://doi.org/10.1016/j.ocemod.2020.101611>

- 427 Puthan, P., Pawlak, G., & Sarkar, S. (2022). Wake Vortices and Dissipation in a Tidally Modulated Flow Past a
428 Three-Dimensional Topography. *Journal of Geophysical Research: Oceans*, 127(8), e2022JC018470.
429 <https://doi.org/10.1029/2022JC018470>
- 430 Rahm, L. (1985). On the diffusive salt flux of the Baltic proper. *Tellus A*, 37A(1), 87–96.
431 <https://doi.org/10.1111/j.1600-0870.1985.tb00272.x>
- 432 Reissmann, J. H., Burchard, H., Feistel, R., Hagen, E., Lass, H. U., Mohrholz, V., Nausch, G., Umlauf, L., &
433 Wieczorek, G. (2009). Vertical mixing in the Baltic Sea and consequences for eutrophication – A review.
434 *Progress in Oceanography*, 82(1), 47–80. <https://doi.org/10.1016/j.pocean.2007.10.004>
- 435 St. Laurent, L. C., Simmons, H. L., & Jayne, S. R. (2002). Estimating tidally driven mixing in the deep ocean:
436 ESTIMATING TIDALLY DRIVEN MIXING. *Geophysical Research Letters*, 29(23), 21-1-21–24.
437 <https://doi.org/10.1029/2002GL015633>
- 438 Stigebrandt, A. (1976). Vertical diffusion driven by internal waves in a sill fjord. *Journal of Physical*
439 *Oceanography*, 6(4), 486–495.
- 440 Stigebrandt, A. (1987). A Model for the Vertical Circulation of the Baltic Deep Water. *Journal of Physical*
441 *Oceanography*, 17(10), 1772–1785. [https://doi.org/10.1175/1520-0485\(1987\)017<1772:AMFTVC>2.0.CO;2](https://doi.org/10.1175/1520-0485(1987)017<1772:AMFTVC>2.0.CO;2)
- 442 van der Lee, E. M., & Umlauf, L. (2011). Internal wave mixing in the Baltic Sea: Near-inertial waves in the absence
443 of tides. *Journal of Geophysical Research*, 116(C10), C10016. <https://doi.org/10.1029/2011JC007072>
- 444 Waterhouse, A. F., MacKinnon, J. A., Nash, J. D., Alford, M. H., Kunze, E., Simmons, H. L., Polzin, K. L., Laurent,
445 L. C. S., Sun, O. M., Pinkel, R., Talley, L. D., Whalen, C. B., Huussen, T. N., Carter, G. S., Fer, I.,
446 Waterman, S., Garabato, A. C. N., Sanford, T. B., & Lee, C. M. (2014). Global Patterns of Diapycnal
447 Mixing from Measurements of the Turbulent Dissipation Rate. *Journal of Physical Oceanography*, 44(7),
448 1854–1872. <https://doi.org/10.1175/JPO-D-13-0104.1>
- 449 Welch, W. T., Smolarkiewicz, P., Rotunno, R., & Boville, B. A. (2001). The large-scale effects of flow over
450 periodic mesoscale topography. *Journal of the Atmospheric Sciences*, 58(12), 1477–1492.
- 451 Wüest, A., & Lorke, A. (2003). Small-Scale Hydrodynamics in Lakes. *Annual Review of Fluid Mechanics*, 35(1),
452 373–412. <https://doi.org/10.1146/annurev.fluid.35.101101.161220>
- 453
454